



# Self-assembled foam-like graphene networks formed through nucleate boiling

SUBJECT AREAS:

SYNTHESIS OF GRAPHENE

SOLAR CELLS

ELECTRONIC PROPERTIES AND DEVICES

MECHANICAL AND STRUCTURAL PROPERTIES AND DEVICES

Ho Seon Ahn<sup>1\*</sup>, Ji-Wook Jang<sup>2\*</sup>, Minsu Seol<sup>2</sup>, Ji Min Kim<sup>3</sup>, Dong-Jin Yun<sup>4</sup>, Chibeom Park<sup>5</sup>, Hyungdae Kim<sup>6</sup>, Duck Hyun Youn<sup>2</sup>, Jae Young Kim<sup>2</sup>, Gunyeop Park<sup>3</sup>, Su Cheong Park<sup>3</sup>, Jin Man Kim<sup>7</sup>, Dong In Yu<sup>3</sup>, Kijung Yong<sup>2</sup>, Moo Hwan Kim<sup>7,3</sup> & Jae Sung Lee<sup>7,2</sup>

<sup>1</sup>Division of Mechanical System Engineering, Incheon National University, Incheon, 406-772, Republic of Korea, <sup>2</sup>Department of Chemical Engineering, POSTECH, Pohang, 790-784, Republic of Korea, <sup>3</sup>Department of Mechanical Engineering, POSTECH, Pohang, 790-784, Republic of Korea, <sup>4</sup>Analytical Engineering Laboratory of Samsung Advanced Institute of Technology, PO Box 111, 440-600, Republic of Korea, <sup>5</sup>Department of Chemistry, POSTECH, Pohang, 790-784, Republic of Korea, <sup>6</sup>Department of Nuclear Engineering, Kyung Hee University, Youngin, 446-701, Republic of Korea, <sup>7</sup>Division of Advanced Nuclear Engineering, POSTECH, Pohang, 790-784, Republic of Korea.

Received  
3 December 2012

Accepted  
11 February 2013

Published  
7 March 2013

Correspondence and requests for materials should be addressed to M.H.K. (mhkim@postech.ac.kr) or J.S.L. (jlee@postech.ac.kr)

\* These authors contributed equally to this work.

Self-assembled foam-like graphene (SFG) structures were formed using a simple nucleate boiling method, which is governed by the dynamics of bubble generation and departure in the graphene colloid solution. The conductivity and sheet resistance of the calcined (400°C) SFG film were  $11.8 \text{ S}\cdot\text{cm}^{-1}$  and  $91.2 \Omega\text{cm}^{-1}$ , respectively, and were comparable to those of graphene obtained by chemical vapor deposition (CVD) ( $\sim 10 \text{ S}\cdot\text{cm}^{-1}$ ). The SFG structures can be directly formed on any substrate, including transparent conductive oxide (TCO) glasses, metals, bare glasses, and flexible polymers. As a potential application, SFG formed on fluorine-doped tin oxide (FTO) exhibited a slightly better overall efficiency (3.6%) than a conventional gold electrode (3.4%) as a cathode of quantum dot sensitized solar cells (QDSSCs).

Graphene has become the focus of extensive studies worldwide since Geim and Novoselov successfully separated the one-atom-thick planar sheet of  $\text{sp}^2$  bonded carbon from graphite using the so-called ‘Scotch tape method’ in 2004<sup>1</sup>. Graphene has unusual characteristics, including outstanding electronic properties<sup>2</sup>, thermal conductivity<sup>3</sup>, optical properties<sup>4</sup>, high mechanical strength<sup>5</sup>, and large surface areas<sup>6</sup>. Due to these unique properties, graphene is useful in transparent electrically conducting films<sup>7</sup>, electrodes of energy storage devices<sup>5,7,8</sup>, field-effect devices<sup>9,10</sup>, microelectronic devices<sup>1</sup>, chemical and biological sensors<sup>11–13</sup>, and fillers in conductive polymeric composites<sup>14</sup>. Most previous research has focused on two-dimensional (2-D) constructs. However, to take full advantage of graphene’s superior physical and electronic properties, large surface area, and chemical functionality, 2-D graphene sheets must be integrated into macroscopic three-dimensional (3-D) structures<sup>15–27</sup>.

Recently, Zhu *et al.* synthesized a continuous, nonporous 3-D network of highly curved ( $\sim 3100 \text{ m}^2\cdot\text{g}^{-1}$ ) graphene through a simple chemical activation of exfoliated graphene oxide (GO)<sup>15</sup>. A supercapacitor with this carbon network exhibits considerably increased gravimetric capacitance ( $100 \sim 120 \text{ F}\cdot\text{g}^{-1}$ ) and energy density ( $\sim 75,000 \text{ W}\cdot\text{kg}^{-1}$ ) compared with organic and ionic liquid electrolytes. Lee *et al.* fabricated macroporous carbon films of reduced graphene oxide (RGO) using the ‘breath-figure’<sup>16,23,28,29</sup> method, which is a well-known technique for synthesizing porous polymer films<sup>16</sup>. Here, hexagonally packed water droplets were spontaneously condensed on the polymer-grafted GO flakes solution in a stream of humid air. The complete evaporation of the solvent and water resulted in the macro-porous film of polymer-grafted GO flakes. However, the synthesis of polymer-grafted GO flakes using this method is time-consuming due to the multi-step processes. Both of these techniques require an additional high-temperature reduction process and a transfer process. Chen *et al.* fabricated 3-D graphene foam using template-directed chemical vapor deposition (CVD)<sup>17</sup>. The optimized conductivity of  $10 \text{ S}\cdot\text{cm}^{-1}$  is  $\sim 6$  orders of magnitude greater than that of chemically derived graphene-based composites<sup>30</sup>; its conductivity is maintained even after filling the pores with polydimethyl siloxane (PDMS). However, the CVD process requires high processing temperatures and etching processes, which require nickel or copper foam to generate the graphene foam. The graphene film also must be transferred onto a foreign substrate, so the process remains expensive and time-consuming.



Herein, we report a simple nucleate boiling method for the direct formation of self-assembled foam-like graphene (SFG) structures on various target substrates without additional transfer or etching processes. The process is governed by the dynamics of bubble generation and departure in the graphene colloid solution and can be regulated by adjusting heat flux and boiling time. Our new method involves a single-step, low-temperature ( $<200^{\circ}\text{C}$ ), low-cost, yet its properties including the conductivity are comparable to those of CVD graphene foam. Since it could be formed on any substrates, there are a wide variety of potential applications. As a cathode for QDSSC, the graphene foam showed the performance even slightly better than the state-of-the-art Au electrode.

## Results

In the nucleate boiling method, a thin substrate can be placed on a heater, or the substrate itself can act as a heater in the graphene colloid solution. In this solution, RGO prepared by Hummer's method<sup>31</sup> and hydrazine reduction<sup>32</sup> is well dispersed by electrostatic repulsion between the negatively charged carboxylic groups on the graphene sheets. More than 90% of the RGO formed monolayers, and atomic force microscopy (AFM) revealed that the RGO sheets in suspended water had thicknesses of  $\sim 0.524$  nm which exceeded that of a single graphene layer (0.334 nm) (Fig. S1 in Supplementary Information). The apparent increase in the height of graphene on mica resulted from residual epoxy and carbonyl groups that had not fully reduced<sup>33</sup>. The RGO colloid solution in a saturated state was boiled under atmospheric conditions on a silicon dioxide ( $\text{SiO}_2$ )-coated silicon heater with a heat flux of  $1200 \text{ kW}\cdot\text{m}^{-2}$  for 10 min. The heat flux and the wall temperature of the heater were controlled by regulating the applied electric voltage.

The formation process of SFG during nucleate boiling was monitored by scanning electron microscopy (SEM). First, 50  $\sim$  100-nm base graphene layers (BGLs) were stacked on the  $\text{SiO}_2$  surface in the boiling RGO solutions (Fig. 1a). The BGLs were assemblies of 2-D RGO platelets, which were composed of 5  $\sim$  10 layers of RGO stacked parallel to the substrate. The RGO platelets retain their hydrophilic characteristic due to the carboxylic acid groups at the edge. In the X-ray photoemission spectroscopy (XPS) survey spectra of GO, RGO peaks at 284.6, 286.5, 287.8, and 289.1 eV were

attributed to the  $\text{C}_{1s}$  peak of C-C, C-O, C=O, and C(O)O. Due to epoxides and hydroxyl groups, the peak at 286.5 eV (C-O) decreased dramatically. However, due to carboxylic groups, the peak at 287.8 eV (C=O) was not reduced as much as the C-O peak (Fig. S2 and Table S1 in Supplementary Information). We also measured the contact angle of the water droplet at the interface between the BGLs and the  $\text{SiO}_2$  substrate, denoted by a red circle in the highly magnified high-resolution SEM (HRSEM) image shown in Fig. 1a. The contact angle of a 1- $\mu\text{L}$  water droplet on BGLs ( $56.3^{\circ}$ ) was even smaller than that on the  $\text{SiO}_2$  substrate ( $72.2^{\circ}$ ), indicating that the BGLs had an extremely high surface wettability (inset in Fig. 1(a)); this is the result of negatively charged carboxylic groups<sup>24</sup>. SFG began to form on the BGL through the self-assembly of RGO platelets, with the aid of bubbles on the substrate (Fig. 1b). Most RGO platelets were in a free-standing form, generating the wall of the SFG pores. The contact angle of the water droplet at this initial stage was  $62.4^{\circ}$ , demonstrating that this film retained its hydrophilic characteristic due to the BGLs just below the SFG seeds. However, as the reaction continued, SFG structures formed, and the water droplet contact angle on the surface of 3-D SFG became  $120.6^{\circ}$ ; thus, the SFG surface was hydrophobic<sup>34,35</sup> (Fig. 1c). These results indicate that the hydrophilic motif (primarily at the end of the RGO platelets) was reduced or buried in the structure during the formation of foam-like graphene. Thus, interactions likely occurred between hydrophilic groups, especially carboxylic acid groups. We believe that self-assembly of RGO platelets occurred through condensation or hydrogen bonding<sup>14,16,36,37</sup> (Fig. 1b); this could be tested in the future using detailed spectroscopic studies<sup>36</sup>.

An interesting phenomenon was observed during the measurement of the water droplet contact angle. Water cannot permeate hydrophobic material with pores or micro/nanoscale structures<sup>38,39</sup>. However, when a 10- $\mu\text{L}$  water droplet was dispersed, it was absorbed in 1 min, as shown in Supplementary Fig. S3a. To further investigate the water absorption phenomenon, we attempted to observe the wetting on the SFG layer using environmental-SEM (E-SEM), as shown in Supplementary Fig. S3b. At  $30^{\circ}\text{C}$  and 0.6 bar, water on the SFG was observed digitally. Water droplets were generated on several points of the SFG layer. Most of the water droplets on the SFG film disappeared, as indicated by red circles in the E-SEM images

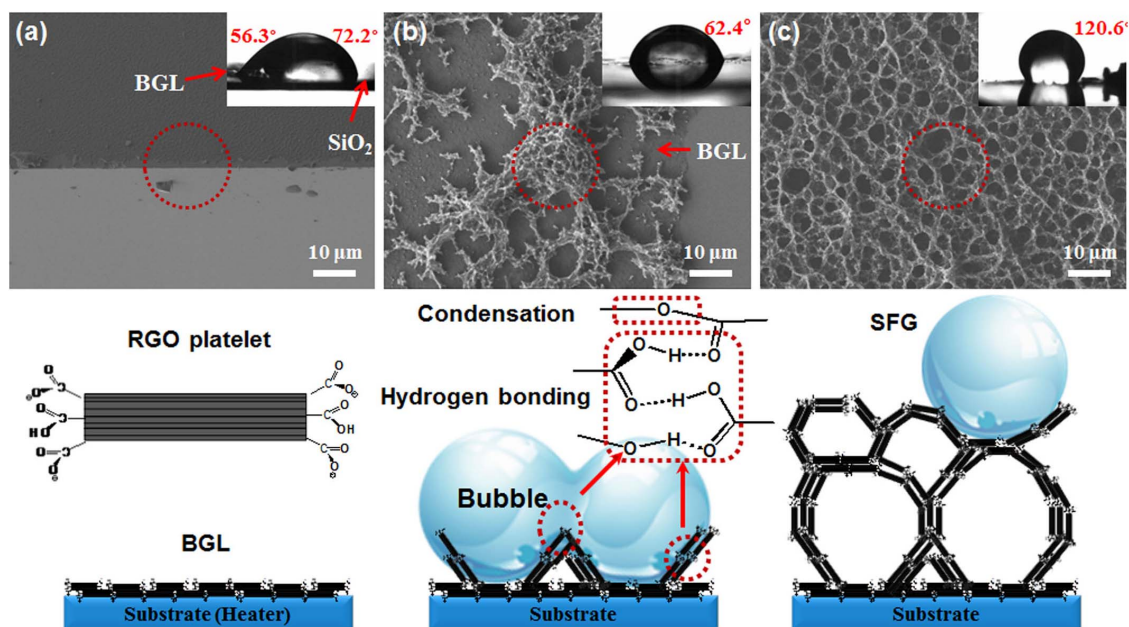


**Figure 1** | Schematic illustrations of 3-D SFG formation: (a) BGL: RGO platelets were stacked in the parallel direction with a thickness of 50–100 nm. (b) The structure of SFG seeds formed on the BGL with the help of bubbles via condensation and hydrogen bonding between RGO platelets (denoted as red circles and boxes), and (c) SFG formation from the seed and bubbles.





(Supplementary Fig. S3b). This result suggests that the SFG layer retained both hydrophobic and hydrophilic properties due to hydrophobic RGO planes exposed to the surface and carboxylic groups buried in the structures by self-assembly<sup>34</sup>. These dual characteristics make it useful as a scaffold in both polar and organic solvents.

The morphology of SFG structures was further investigated using HRSEM and high-resolution transmission electron microscopy (HRTEM) analysis (Fig. 1, 2 and Supplementary Fig. S4). Figure 2a–c shows SEM images of SFG structures at different magnifications, and Fig. 2d shows an AFM image. The pore size varied over a range of 1–5  $\mu\text{m}$ , and many small pores were observed. RGO platelets were well interconnected, forming the walls of the SFG pores. Additionally, many free-standing RGO platelets were found in the SFG structures (Fig. 2e), providing strong evidence for the SFG formation mechanism described above. The RGO platelets were composed of 5–10 graphene layers, and the interlayer spacing was 3.52  $\text{\AA}$ , as observed by HRTEM (Fig. 2f). The average thickness of the SFG structures was  $\sim 9.3 \mu\text{m}$ , and the thickness of the BGL was  $\sim 100 \text{ nm}$  (Supplementary Fig. S4a). The BGL below the SFG structures plays very important roles. A 2-D BGL can act as a reservoir for electrons from 3-D SFG structures, which induces efficient charge transfer, especially on a non-conducting substrate. Supplementary Figure S4b shows the side-view HRSEM image of an SFG film. The pore size was 1–3  $\mu\text{m}$ , similar to the pores viewed horizontally. The sheet resistance and conductivity of the SFG film on the  $\text{SiO}_2$  coated silicon substrate was measured by the four-point probe method. The sheet resistance of the  $\text{SiO}_2$  coated silicon substrate was too high to measure using a multimeter, indicating that the sheet resistance of the substrate exceeded  $500 \text{ M}\Omega \square^{-1}$ . The sheet resistance of SFG was measured ten times and the average value was  $6.7 \text{ S}\cdot\text{cm}^{-1}$ , slightly lower than that of CVD-derived foam-like graphene ( $\sim 10 \text{ S}\cdot\text{cm}^{-1}$ ; an optimized conductivity by controlling the average number of graphene layers). However, when the film was annealed at  $400^\circ\text{C}$

in an argon atmosphere, the conductivity increased to  $11.8 \text{ S}\cdot\text{cm}^{-1}$  ( $91.2 \Omega \square^{-1}$  sheet resistance), which was even higher than that of the CVD-derived graphene foam (Table 1). Because nucleate boiling also reduces the RGO platelets, the conductivity enhancement due to annealing was not as great as in the case of 2-D RGO<sup>40</sup>.

The conductivity of chemically derived SFG structures is determined mainly by the resistance of RGO itself and the resistance between the RGO platelets. As mentioned above, RGO platelets likely self-assemble via condensation and hydrogen bonding between their carboxylic groups. The interaction between the self-assembled platelets was so strong that it prevented detachment of the SFG film, even with ‘Scotch tape’ and sonication in water. Resistance between platelets was minimized due to the short distance and strong interaction between RGO platelets. Nucleate boiling further reduced the RGO platelets by thermal reduction<sup>41</sup>, as explained previously. The  $(\text{C-C} + \text{C}=\text{C})/(\text{C-O} + \text{C}=\text{O} + \text{C}(\text{O})\text{O})$  ratio of GO (1.1) was increased in RGO (1.8) and in SFG (2.1) by the restoration of  $\text{sp}^2$  domains (Table S1). This result indicates that further reduction took place during nucleate boiling<sup>32,42</sup>.

The XPS results were confirmed using Raman spectroscopy, which revealed that the  $I_D/I_G$  ratio of GO (0.88) increased to 1.16 (RGO) and to 1.43 (SFG) (Fig. 3a and Supplementary Table S2). The G band (at  $1600 \text{ cm}^{-1}$ ) and D band (at  $1354 \text{ cm}^{-1}$ ) originate from the  $E_{2g}$  mode of the aromatic carbon rings and disorders such as ripples, edges, and defects, respectively. Pure graphene, prepared using the ‘Scotch tape’ method or direct exfoliation of graphite, has a much more intense G band compared with its D band. However, RGO typically exhibits similar intensity for both bands, indicating that the degree of disorder increases during reduction, despite restoration of the 6-fold aromatic rings<sup>43,44</sup>. After nucleate boiling, the degree of disorder was further increased through additional thermal reduction. Ultraviolet photoemission spectroscopy (UPS) investigation of GO, RGO, and SFG films were conducted to further investigate the bonding state and the degree of reduction. In the valence band structure, the peak intensity around the Fermi energy ( $E_F$ ) reveals the metallic property of the material (Fig. 2b). When GO was reduced to RGO, the peak intensity increased due to  $\text{sp}^2$  bond restoration, but the peak intensity of SFG was even higher than that of RGO due to nucleate boiling. The secondary cut-off region ( $E_{\text{cutoff}}$ ) and  $E_F$  were clearly defined, and the work function of each film was calculated using equation (1)<sup>2,42</sup>:

$$\phi = h\nu - E_{\text{cutoff}} + E_{\text{Fermi}} \quad (1)$$

where  $h\nu$  (40.8 eV) is the incoming photon energy from the He II source. A bias of  $-5 \text{ V}$  was applied to create a clear boundary in the  $E_{\text{cutoff}}$  region. However, in the case of GO film, the  $E_{\text{cutoff}}$  could not be measured due to charging on the surface of the film. The work function of the conductive film depends strongly on the surface properties as well as bulk properties. The reported work function values for graphene are 4.2–4.5 eV<sup>41</sup>. The measured work functions for RGO and SFG were 4.55 eV (4.90 eV: calculated by Kelvin probe) and 4.30 eV (4.78 eV) respectively, verifying that SFG was further

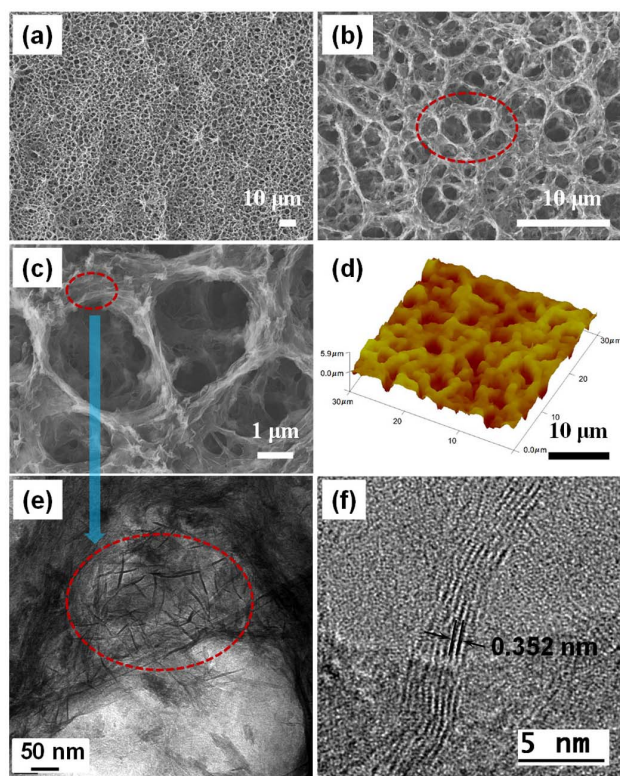


**Figure 2** | The morphology of the 3-D SFG structure: (a) – (c) Low and high-magnification of SEM image of SFG. (d) AFM image of SFG. (e) HRSEM image on the junction of the pores. (f) HRTEM image for RGO platelets.

Table 1   The Sheet resistance and conductivity of GO, SFG and SFG-A		
Sample	Resistance ( $\Omega \square^{-1}$ )	Conductivity ( $\text{S cm}^{-1}$ )
GO	$>500 \text{ M}\Omega \square^{-1}$	-
SFG	161.1	6.7
mSFG-A [a]	$91.2 \pm 0.088 \text{ (s.d.)}$	11.8
	$\pm 0.021 \text{ (s.d.)}$	

[a] SFG-A: Calcined SFG film at  $400^\circ\text{C}$  for 4 h under argon.

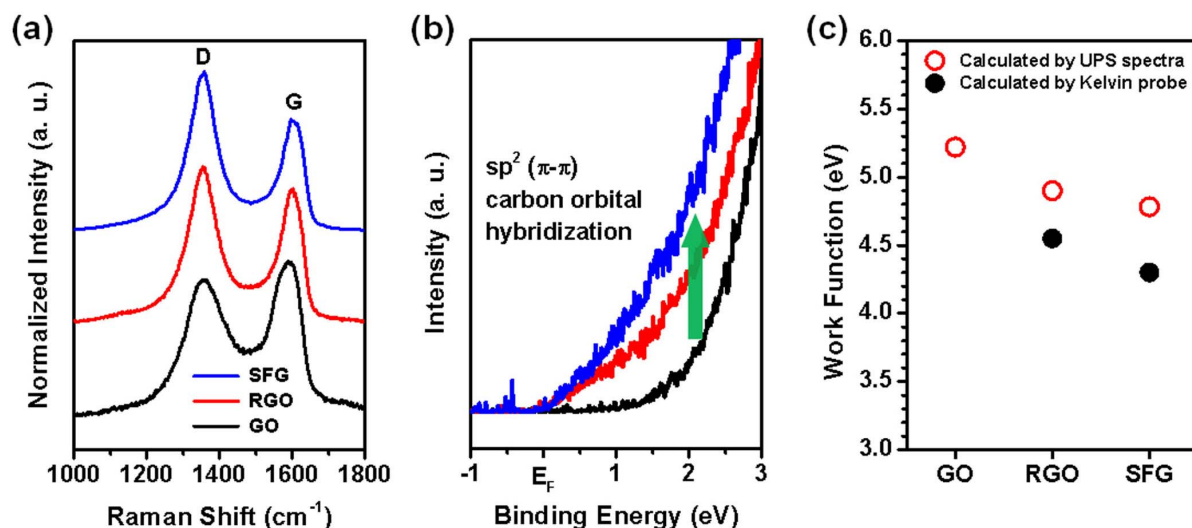


**Figure 3** | Characterization of SFG: (a) Raman spectra. (b) UPS spectra. and (c) Work function of GO, RGO, and SFG.

reduced compared to RGO. Decreasing the number of electron withdrawing groups, such as -OH, -O-, and -COOH, on RGO would reduce the work function. Based on the decreased work function and the increased  $(C-C \text{ or } C=C)/(C-O + C=O + C(O)O)$  and  $I_D/I_G$  ratios, we concluded that RGO was further reduced during nucleate boiling. Due to the good connectivity and further  $sp^2$  bond restoration, the conductivity of the SFG became comparable to that of SFG synthesized by CVD methods, even though it was essentially a chemically reduced graphene, like RGO.

Next, we considered how the BGLs and SFG structures formed on the surface of the heater. First, we investigated the interaction between the heater and the RGO colloid solution by regulating the heat flux. Heat flux was increased step-by-step to maintain a steady state (Fig. 4a). At a heat flux of  $50 \text{ kW}\cdot\text{m}^{-2}$  (below the onset of the nucleate boiling point,  $T = 112^\circ\text{C}$ ), no graphene was found on the heater even with increasing heating time. Thus, the generated bubbles by nucleate boiling are essential for the formation of RGO on a heater (a heated substrate). From the classic and the recent literatures, the life-cycle of a bubble by the nucleate boiling from liquid to vapor was revealed as bubble generation, bubble growth, and departure. In general, the bubble could be generated above the onset of nucleate boiling (ONB); i.e. when the bubble on the heater surface starts to be generated at the certain heat flux and wall temperature. From this moment, the life-cycle of bubble could be defined by the single bubble generation, growth, and departure. (When the heat flux increases, the nucleation sites density of bubble also increases. At every nucleation site, the life-cycle of bubbles is repeated with the given heat flux. When the heat flux was increased to  $100 \text{ kW}\cdot\text{m}^{-2}$  (slightly above the ONB point,  $T = 115^\circ\text{C}$ ), single bubble generation at the isolated nucleation site started (Fig. 4b). During repeated generation, growth, and departure of bubble, a liquid film (micro-layer, a few micrometers thick) beneath the bubbles induced horizontal alignment of graphene to form BGLs<sup>45–47</sup>. As the bubbles expanded during the growth, the triple line (where vapor–liquid–solid phases meet) moved, forming BGLs along the micro-layer (Supplementary Fig. S5a, S6a and S7). The movement of triple line during the single bubble growth was validated by the high speed visualization and the infrared radiography (IR) of the heater substrate. The black-colored circle by the heater surface of infrared radiography is larger as the time increases from 0 to 6 ms (Fig S5a).

At  $200 \text{ kW}\cdot\text{m}^{-2}$ , the main nucleation site was formed with the RGO structure (Supplementary Fig. S6). At the end of concentric circles of BGL, the folded RGO sheets were observed, which would

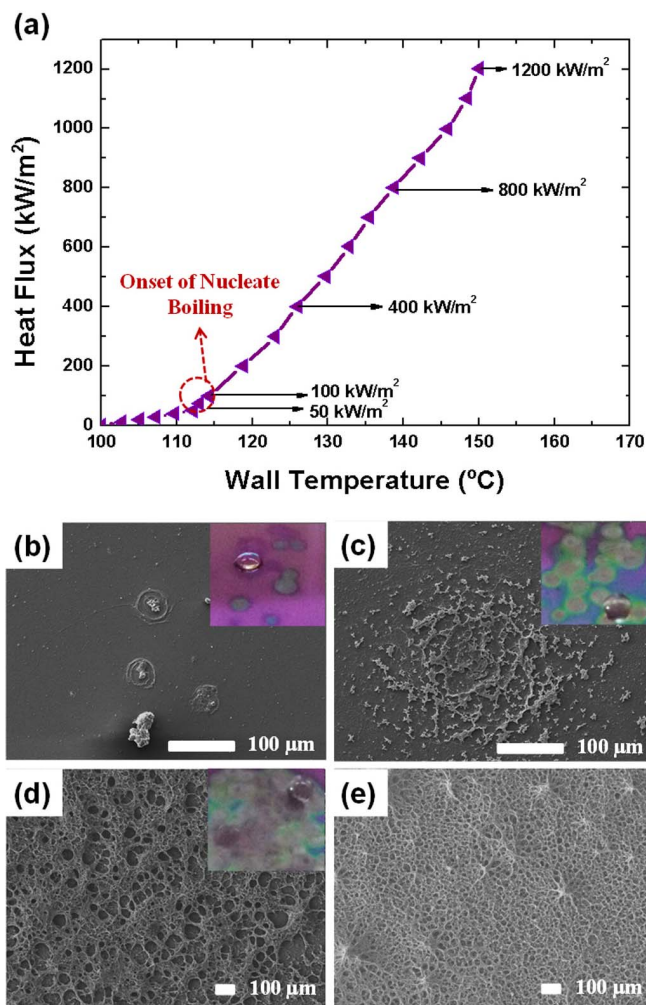


**Figure 4** | Nucleate boiling experiments: Boiling curve represented by the applied heat flux ( $q''$ ) and the wall temperature ( $T_{\text{wall}}$ ). Bubble and SFG formation state at (a)  $100 \text{ kW}/\text{m}^2$ : 2–4 nucleation sites. (b)  $400 \text{ kW}/\text{m}^2$ : start the merge of bubbles. (c)  $800 \text{ kW}/\text{m}^2$ : SFG. and (d)  $1200 \text{ kW}/\text{m}^2$ : SFG, respectively.





act as the seed of SFG, because the rougher structure can provide more change of bubble nucleation. In addition, as the heat flux increases, the nucleate site density (the locations of single bubble generation) increased too. Thus, the BGLs at every nucleate site could cover the entire heater substrate. At  $400 \text{ kW}\cdot\text{m}^{-2}$ , more bubbles were generated, and some merged into larger ones as they expanded and departed, which is called the bubble coalescence phenomenon. The concentration of RGO platelets at the local vacancy between the bubbles increased suddenly, so the RGO platelets were compressed, forming the seed for the SFG structures<sup>48,49</sup> (Figures S5b and S6b). The SEM images in Figure S5b and S6 show that the BGLs and the seed for SFG formed a concentric circle with the nucleation site as its center. In addition, the local vacancy during the coalescence was also validated by the high speed visualization and the IR of the heater substrate (Supplementary Fig. S5b). The vacancy between bubbles during merging could be observed as the white line between large and small black-colored circles. This vacancy would provide the suppression pressure to downward, and the RGO flakes were instantly stacked on the BGL for the seed of SFG. The insets in Fig. 4b–e show that BGLs and the seed for SFG were deposited on the surface of the substrate only where bubbles were generated, providing support for the mechanism discussed above.

At the high heat flux region ( $800$  and  $1200 \text{ kW}\cdot\text{m}^{-2}$ ), many small bubbles were generated, covering the entire heater and merging together. These conditions generated SFG structures with relatively small and uniform pores (Fig. 4d,e). The results demonstrate that the pore size of SFG can be tuned by regulating the heat flux. However, at a low heat flux (below  $800 \text{ kW}\cdot\text{m}^{-2}$ ), more time (i.e., hours) was required to fabricate the SFG structures, and it was difficult to obtain uniform pores (Fig. 4d). Thus, we used the system that allows a higher flux to form SFG with much smaller and uniform pores in a shorter time (i.e., seconds to minutes). At the high heat flux region, the pore size of SFG is in a good agreement with the one predicted by the classical nucleate boiling theory<sup>50</sup>, i.e. the smallest cavity on the heater that could generate bubble at the given heat flux. The cavity theory for the bubble generation is thermodynamically derived as follows.

$$r^* = \left( \frac{2\sigma T_{\text{sat}} v_g k_l}{q'' i_{\text{fg}}} \right)^{1/2} \quad (2)$$

where  $r^*$ ,  $\sigma$ ,  $T_{\text{sat}}$ ,  $v_g$ ,  $k_l$ ,  $q''$ , and  $i_{\text{fg}}$  are the size of active cavity, the surface tension, the saturated temperature of liquid, the specific

volume of vapor, the thermal conductivity of liquid, the applied heat flux, and the latent heat, respectively. According to Eq. 2, the active cavity size for bubble generation at the heat flux of  $1200 \text{ kW}\cdot\text{m}^{-2}$  is nearly  $4 - 5$  micro meters, which is the same as the pore size of our SFG. In addition, when the nucleate boiling time increased from  $10$  to  $60$  min,  $9.3$  and  $42.2$ - $\mu\text{m}$ -thick SFG films were obtained at  $1200 \text{ kW}\cdot\text{m}^{-2}$ , respectively. Thus, pore size and film thickness are tunable by adjusting heat flux and boiling time. Finally, a simple schematic of SFG preparation process was provided by the nucleate boiling in RGO colloid with heat flux up to  $1200 \text{ kW}\cdot\text{m}^{-2}$ . (Figure S8)

Based on the above mechanism, we expect that the SFG structure can be deposited on any substrate, including TCO glasses (FTO), metals (copper), bare glasses, and polymers (PDMS), without requiring surfactants or additional procedures such as etching, polymer removal, or SFG transfer. It was easy to fabricate SFG structures on conducting substrates like FTO and copper (Fig. 5a,b). Even on non-conducting substrates such as glass or PDMS, it was possible to fabricate SFG structures when the substrates were in good contact with the heater (Fig. 5c, d). SEM analysis confirmed the formation of SFG structures on each substrate, and it was easy to scale up the process in all cases. The thickness of SFG-coated PDMS was greater than  $6$  cm (Fig. 5d). With the exception of copper, which is intrinsically opaque (not transparent), all films showed semi-transparent characteristics, despite their micro-scale thicknesses ( $\sim 10 \mu\text{m}$ ). The pores within the SFG structure afforded the semi-transparent characteristics. Thus SFG could be formed on any substrates that can transfer heat; hard or flexible, conducting or non-conducting, metals, semiconductors, or glasses, etc.

The facile formation of SFG on a variety of substrates promises its versatile applications. As an example, we applied SFG-loaded FTO as the counter electrode of quantum dot sensitized solar cells (QDSSCs). In our system, we used CdS and CdSe as visible-light absorbing QDs, and ZnO nanowires acted as an electron collector as well as an absorbent layer (Fig. 6a). Electrons produced by light irradiation on CdSe ( $1.7 \text{ eV}$ ) and CdS ( $2.4 \text{ eV}$ ) are injected into the conduction band of ZnO, and holes moved in the opposite direction through the valence bands, finally oxidizing the polysulfide mediator (inset in Fig. 6a). Rare and expensive Pt or Au catalysts deposited on FTO are commonly used as counter electrodes. We used SFG on FTO as an alternative noble-metal-free counter electrode, and fabricated highly efficient CdSe/CdS/ZnO nanowire-based QDSSCs. The

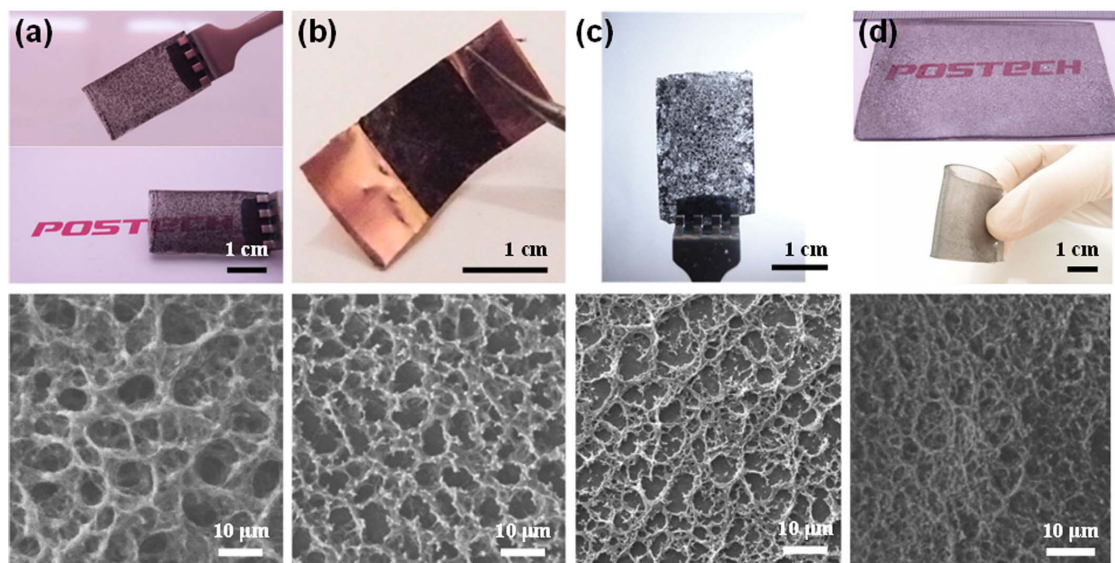


**Figure 5** | SFG on various substrates: SEM image and picture of SFG film on: (a) FTO glass. (b) Copper foil. (c) Glass. and (d) PDMS.

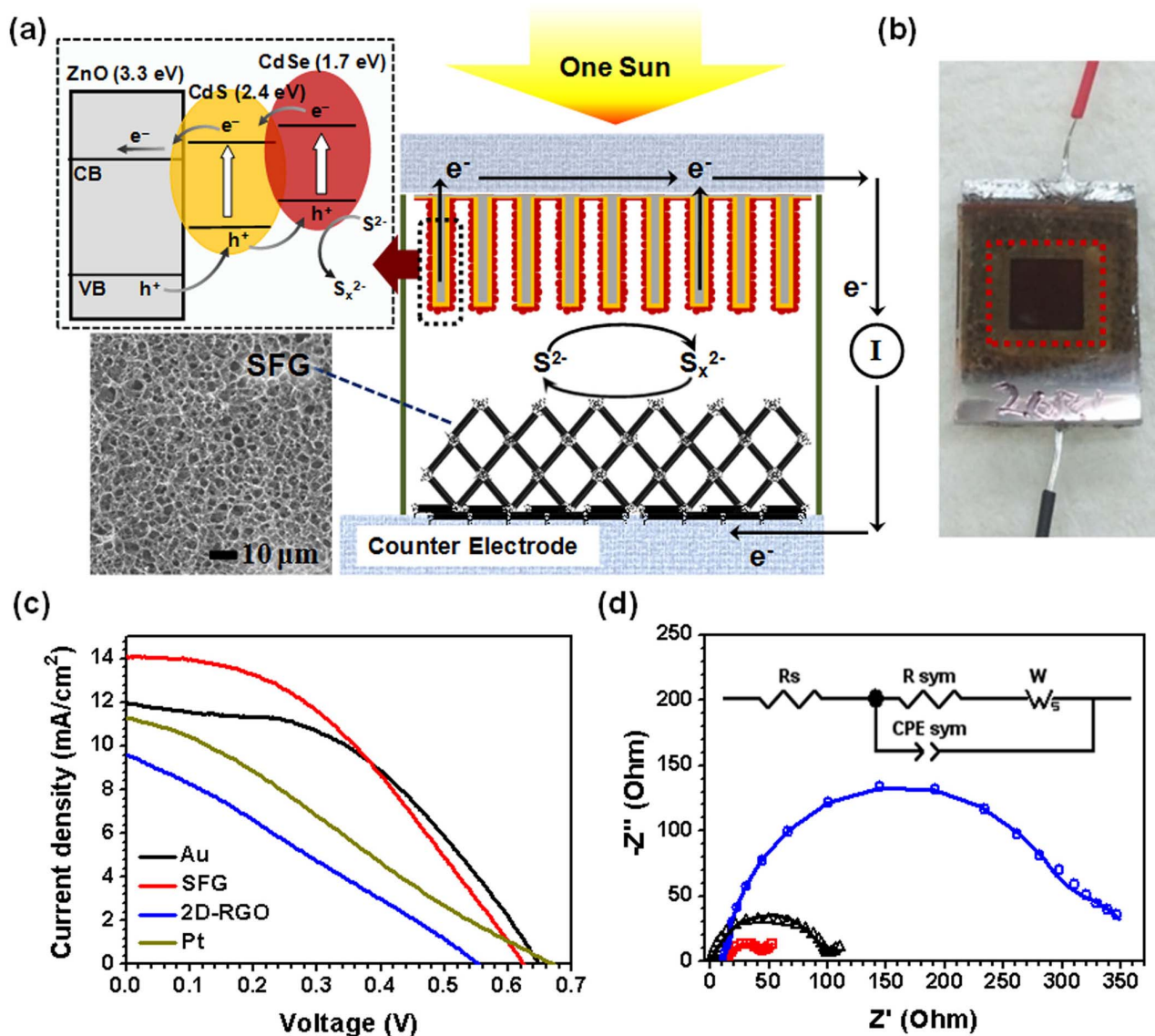


**Figure 6** | SFG-based QDSSCs: (a) Schematic diagram of SFG-based QDSSCs. (b) Schematic and real image of SFG-based QDSSCs. (c) Performance of Au-, 2-D-RGO-, and SFG-based QDSSCs. (d) Electrochemical impedance spectra (Nyquist plots).

well-interconnected, macroporous SFG framework provided an extremely satisfactory surface area, and its superior wettability would facilitate diffusion and charge transfer in the electrolyte. Fig. 6b shows a scheme of SFG-based QDSSCs; the red dotted box indicates an active area containing the CdSe/CdS/ZnO nanowire system ( $0.25 \text{ cm}^2$ ). For comparison, we also prepared Au, Pt and 2-D RGO-based QDSSCs. Basic  $J$ - $V$  characteristics of CdSe/CdS-cosensitized ZnO nanowire solar cells using Au, Pt, 2-D RGO, or SFG as the counter electrode in Fig. 6c were measured under a simulated air mass 1.5 global (AM 1.5G) sunlight using a polysulfide electrolyte. Table 2 lists detailed photovoltaic parameters (open-circuit voltage ( $V_{oc}$ ), short-circuit current density ( $J_{sc}$ ), fill factor (FF), and  $\eta$ ) for each sample. The cell with SFG as the counter electrode yielded the highest  $\eta$  of 3.6%, and  $V_{oc}$ ,  $J_{sc}$ , and FF were measured to be 624 mV,  $14.1 \text{ mA} \cdot \text{cm}^{-2}$ , and 0.42, respectively, using a mask to shield the light from the other areas. The cells with counter electrodes of Au, Pt and 2-D RGO yielded lower  $\eta$  values of 3.4, 2.0 and 1.4%, respectively. The  $\eta$  value of Pt is lower than that of Au due to the deactivation resulting from strong adsorption of sulfur compounds<sup>51</sup>.

To investigate the origin of the high  $\eta$  of the QDSSC with SFG as the counter electrode, electrochemical impedance spectra (EIS) of

SFG, Au, and 2-D RGO counter electrodes were measured in a symmetric cell configuration consisting of two identical counter electrodes<sup>52</sup>. Fig. 6d presents the EIS results in the form of Nyquist plots. Here, the  $x$ -axis represents the real part of the measured impedance, and the  $y$ -axis represents the negative number of the imaginary part of the measured impedance. The small dots in the plot represent the experimental data for the equivalent circuit model. The solid line was fitted by ZSimpWin software using the proposed equivalent circuit model. The Nyquist plot represents the charge transfer kinetics of the counter electrode<sup>53</sup>. We selected the Randles–Ershler model, in which  $R_s$  is the ohmic internal resistance, CPE is the capacitance

**Table 2** | Photovoltaic properties of QDSSCs with different counter electrodes (Au, SFG, 2-D RGO)

Sample	$V_{oc}$ (mV)	$J_{sc}$ ( $\text{mA} \cdot \text{cm}^{-2}$ )	FF	$\eta$ (%)
Au	675	12.4	0.40	3.4
SFG	624	14.1	0.40	3.6
2-D RGO	555	9.6	0.27	1.4
Pt	671	11.3	0.27	2.0





phase element for the semiconductor || electrolyte interface, and  $R_{ct}$  is the charge-transfer resistance across the interface. The semi-circle in the high-frequency region corresponds to the charge-transfer process at the electrolyte/electrode interface<sup>52</sup>. The simulated chemical capacitance CPE values were 2484, 346, and 180  $\mu\text{F}$  for SFG, Au, and 2-D RGO, respectively. The fitted CPE value was about 7 times and 14 times larger than those of Au and 2-D RGO, which demonstrates the large active surface area and corresponding chemical capacitance charging/discharging characteristics at the porous electrode/electrolyte interface<sup>54</sup>. The charge-transfer resistance  $R_{ct}$  in SFG and 2-RGO was 14.0 and 144.5  $\Omega\text{cm}^{-2}$ , respectively. The  $R_{ct}$  value of SFG was much lower than that of Au (48.5  $\Omega\text{cm}^{-2}$ ) due to its large active surface area. Due to the dual wettability of the SFG structures, the electrolyte can freely penetrate into the SFG pores. Thus, we were able to use the entire surface area of SFG structures. Also, the good connectivity between RGO platelets facilitated charge transfer through the polysulfide electrolyte. However, 2-D RGO can only utilize the exposed surface area because of the 2-D horizontal stacking of graphene platelets. Furthermore, SFG had much better conductivity than RGO, as mentioned previously. As a result,  $\eta$ ,  $J_{SC}$ , and FF values were much higher for cells with SFG than those with 2-RGO, and even exhibited slightly better cell performance than the reference cell with the state-of-the-art Au electrode (Au). Efficiency could be further enhanced by controlling the pore size and thickness of the SFG film. In the case of CVD-grown foam-like graphene, the hydrophobic nature would prevent electrolyte permeation, as mentioned above.

## Discussion

We demonstrated that 3-D SFG can be easily formed directly on any substrate, including TCO glasses, various metals, bare glasses, and polymers, through nucleate boiling without further processing like transfer. The SFG structures were fabricated by self-assembly of RGO platelets with the aid of bubbles. XPS, Raman, and UPS analyses confirmed that nucleate heating further reduces the RGO. The  $(C-C \text{ or } C=C)/(C-O + C=O + C(O)O)$  and  $I_D/I_G$  ratios of SFG were higher and the work function was lower compared with RGO. The sheet resistance and conductivity of the film were 91.2  $\Omega\text{cm}^{-1}$  and 11.8  $\text{S}\cdot\text{m}^{-1}$ , respectively, comparable to the values of the graphene foam fabricated by CVD. The SFG cathode exhibited promising electrocatalytic activity toward the polysulfide redox couple in QDSSCs; it was even slightly better than the state-of-the-art Au counter electrode and superior to the 2-D RGO cell due to the extremely high surface area and good connectivity as well as facile diffusion of the redox couple. The SFG counter electrode exhibited the best photovoltaic performance, with maximum  $\eta$ ,  $V_{OC}$ ,  $J_{SC}$ , and FF values of 3.60%, 624 mV, 14.1  $\text{mA}\cdot\text{cm}^{-2}$ , and 0.41, respectively. Nucleate boiling is a simple and inexpensive method for fabricating SFG structures on the various substrates and can be easily scaled up. The SFG structures on various substrates could be applied in many fields, including flexible electronics, energy storage devices (especially supercapacitors), chemical and biological sensors, and scaffolds for DSSCs or photoelectrochemical cells.

## Methods

**Preparation of SFG structures.** Nucleate boiling was performed using a pool-boiling experimental facility, which consisted of a pool chamber with saturated water, a reflux condenser, a pre-heater (400 W), and a heater/substrate at the bottom (Supplementary Fig. S9a). The pre-heater was used to remove the dissolved gas in the RGO colloid solution. A silicon substrate (20 × 25 mm) with a  $\text{SiO}_2$  top layer acted as the heater, and the heating element was a Pt thin film with a thickness of about 1200 Å, layered onto the bottom of the substrate using an e-beam evaporator (Supplementary Fig. S9b). Pt film patterns behind the heater and the  $\text{SiO}_2$  coating were necessary to determine the exact wall temperature (substrate temperature) and the applied heat flux, which were essential to monitor SFG formation (Fig. 4). Before the pool-boiling experiment (SFG coating), Pt film patterns behind the silicon heater were calibrated in a convection oven (JEIO TECH, OF-12GW) in order to measure the resistance of the Pt film pattern using a four-wire method at temperatures of 100, 120, 140, and 160°C. A linear calibration curve ( $R^2 \sim 0.99999$ ) for temperature versus

resistance was used to estimate the wall temperature of the silicon heater during the pool-boiling experiment. As shown by the red dotted box in Supplementary Fig. S9a, nucleate boiling on the substrate heater occurred at a heat flux of 300  $\text{kW}\cdot\text{m}^{-2}$ . The RGO colloid solution was prepared at 0.0005 wt% in distilled water. After the preparation process described above, the heat flux was increased step-by-step in increments of 50  $\text{kW}\cdot\text{m}^{-2}$  to maintain a steady state. The heat flux at each step was regulated for 2 min and continuously increased to 1200  $\text{kW}\cdot\text{m}^{-2}$ . SFG structures were coated onto copper, FTO, glass, and PDMS without the  $\text{SiO}_2$  coating or the Pt film pattern. The FTO (40 × 15 mm) was prepared, and SFG formed on FTO at a heat flux of 600  $\text{kW}\cdot\text{m}^{-2}$  for 2 h, using direct heating. Copper foil (Aldrich, 349208-33G) with an area of 10 × 12 mm was prepared, and SFG formed on copper foil under the same conditions as on FTO. We used indirect heating for the non-conductive substrates, PDMS and glass.

### Preparation of CdSe/CdS/ZnO nanowire photoelectrodes and cell fabrication.

CdSe/CdS/ZnO nanowire arrays were prepared using a three-step solution-based method<sup>55</sup>. Arrays of ZnO nanowires, grown on FTO substrates (TEC, 13  $\Omega\text{cm}^{-1}\cdot\text{sq}^{-1}$ ) by an ammonia solution method, were immersed in an aqueous solution containing 0.01 M  $\text{Zn}(\text{NO}_3)_2\cdot 6\text{H}_2\text{O}$  and 0.5 M  $\text{NH}_4\text{OH}$  for 20 h at 95°C. ZnO nanowire electrodes were *in-situ* sensitized with CdS and CdSe using successive ion layer adsorption and reaction (SILAR) and chemical bath deposition (CBD), respectively. The counter electrode and photoelectrode (active area 0.25  $\text{cm}^2$ ) were sandwiched between a 60- $\mu\text{m}$ -thick hot-melt ionomer film (Surllyn) under heating (130°C, 1 min). Polysulfide electrolyte was injected via pre-drilled holes in the counter electrode, and each hole was sealed using a small piece of Surllyn and a microscope cover glass. The polysulfide used here consisted of 0.5 M  $\text{Na}_2\text{S}$ , 2 M S, and 0.2 M KCl (photocurrent density voltage characteristics of the QDSSCs were measured under a simulated air mass 1.5 G solar spectrum).

**Characterization.** The morphologies of the SFG samples synthesized using an alternating-current (AC) power supply were observed using a field-emission scanning electron microscope (SEM, XL30S, Philips), and the detailed microscopic structure was observed using Cs-corrected high-resolution scanning transmission electron microscopy (Cs-corrected HR-[S]TEM, Jeol, JEM 2200FS, 200 kV) at the National Center for Nanomaterials Technology at POSTECH. The contact angle was measured using a high-resolution digital camera and the cold spot light system at the Two-Phase Flow Laboratory at POSTECH. The absorption of water droplets into SFG was observed using the environmental scanning electron microscope (E-SEM) mode of SEM (Quanta 200, FEI) at UNIST. Detailed morphology and height information were obtained using an atomic force microscope (AFM, Nanoscope IIIa, Digital Instrument, Inc.). Raman spectra were acquired using a commercial Raman spectroscope (Alpha 300R, WITEC) equipped with a 532-nm diode laser. Both the AFM and Raman studies were conducted at the Nanoscale Materials Research Laboratory at POSTECH. The bonding state and work function of each film were investigated using X-ray photoemission spectroscopy (XPS) and ultraviolet photoemission spectroscopy (UPS). The resistivity of each film was measured by the four-point probe method (KEITHLEY 2000). Electrochemical impedance spectra (EIS) were measured in a symmetric cell configuration with two identical counter electrodes. The frequency range was from 100 kHz to 100 mHz with an AC modulation signal of 10 mV and bias DC voltage of 0.0 V.

- Novoselov, K. S. *et al.* Electric field effect in atomically thin carbon films. *Science* **306**, 666–669 (2004).
- Geim, A. K. & Novoselov, K. S. The rise of graphene. *Nature Mat.* **6**, 183–191 (2007).
- Balandin, A. A. *et al.* Superior thermal conductivity of single-layer graphene. *Nano Lett.* **8**, 902–907 (2008).
- Kuzmenko, A. B., van Heumen, E., Carbone, F. & van der Marel, D. Universal optical conductance of graphite. *Phys. Rev. Lett.* **100**, 117401 (2008).
- Stoller, M. D., Park, S., Zhu, Y., An, J. & Ruoff, R. S. Graphene-based ultracapacitors. *Nano Lett.* **8**, 3498–3502 (2008).
- Niyogi, S. *et al.* Solution properties of graphite and graphene. *J. Am. Chem. Soc.* **128**, 7720–7721 (2006).
- Wu, Q., Xu, Y. X., Yao, Z. Y., Liu, A. R. & Shi, G. Q. Supercapacitors based on flexible graphene/polyaniline nanofiber composite films. *ACS Nano* **4**, 1963–1970 (2010).
- Wang, Y. *et al.* Supercapacitor devices based on graphene materials. *J. Phys. Chem. C* **113**, 13103–13107 (2009).
- Gilje, S., Han, S., Wang, M., Wang, K. L. & Kaner, R. B. A chemical route to graphene for device applications. *Nano Lett.* **7**, 3394–3398 (2007).
- Luo, Z. T., Lu, Y., Somers, L. A. & Johnson, A. T. C. High yield preparation of macroscopic graphene oxide membranes. *J. Am. Chem. Soc.* **131**, 898–899 (2009).
- Fowler, J. D. *et al.* Practical chemical sensors from chemically derived graphene. *ACS Nano* **3**, 301–306 (2009).
- Lu, C. H., Yang, H. H., Zhu, C. L., Chen, X. & Chen, G. N. A graphene platform for sensing biomolecules. *Angew. Chem. Int. Ed.* **48**, 4785–4787 (2009).
- Shan, C. S. *et al.* Direct electrochemistry of glucose oxidase and biosensing for glucose based on graphene. *Anal. Chem.* **81**, 2378–2382 (2009).
- Dikin, D. A. *et al.* Functionalized graphene sheets for polymer nanocomposites. *Nature* **448**, 457–460 (2007).



15. Zhu, Y. *et al.* Carbon-based supercapacitors produced by activation of graphene. *Science* **332**, 1537–1541 (2011).
16. Lee, S. H. *et al.* Three-dimensional self-assembly of graphene oxide platelets into mechanically flexible macroporous carbon films. *Angew. Chem. Int. Ed.* **49**, 10084–10088 (2010).
17. Chen, Z., Ren, W., Gao, L., Liu, B., Pei, S. & Cheng, H.-M. Three-dimensional flexible and conductive interconnected graphene networks grown by chemical vapor deposition. *Nature Mater.* **10**, 424–428 (2011).
18. Li, C. & Shi, G. Three-dimensional graphene architectures. *Nanoscale* **4**, 5549–5563 (2012).
19. Yin, S., Niu, Z. & Chen, X. Assembly of graphene sheets into 3D macroscopic structures. *Small* **8**, 2458–2463 (2012).
20. Niu, Z., Chen, J., Huey, H. H., Ma, J. & Chen, X. A leavening strategy to prepare reduced graphene oxide. *Adv. Mater.* **24**, 4144–4150 (2012).
21. Worsley, M. A. *et al.* Mechanically robust 3D graphene macroassembly with high surface area. *Chem. Comm.* **48**, 8428–8430 (2012).
22. Yang, X., Zhu, J., Qiu, L. & Li, D. Bioinspired effective prevention of restacking in multilayered graphene films: Towards the next generation of high-performance supercapacitors. *Adv. Mater.* **23**, 2833–2838 (2011).
23. Yin, S. *et al.* Assembly of graphene sheets into hierarchical structures for high-performance energy storage. *ACS Nano* **5**, 3831–3838 (2011).
24. Liang, Q., Yao, X., Wang, W., Liu, Y. & Wong, C. P. A. Three-dimensional vertically aligned functionalized multilayer graphene architecture: An approach for graphene-based thermal interfacial materials. *ACS Nano* **5**, 2392–2401 (2011).
25. Pham, H. D. *et al.* Synthesis of chemically converted graphene xerogel with superior electrical conductivity. *Chem. Comm.* **47**, 9672–9674 (2011).
26. Worsley, M. A. *et al.* Synthesis of graphene aerogel with electrical conductivity. *J. Am. Chem. Soc.* **132**, 14067–14069 (2011).
27. Xu, Y., Sheng, K. & Shi, G. Self-assembled graphene hydrogel via a one-step hydrothermal process. *ACS Nano* **4**, 4324–4330 (2010).
28. Widawski, G., Rawiso, M. & Francols, B. Self-organized honeycomb morphology of star-polymer polystyrene films. *Nature* **369**, 387–389 (1994).
29. Böker, A. *et al.* Hierarchical nanoparticle assemblies formed by decorating breath figures. *Nature Mater.* **3**, 302–306 (2004).
30. Stankovich, S. *et al.* Graphene-based composite materials. *Nature* **442**, 282–286 (2006).
31. Hummers, W. S. & Offeman, R. E. Preparation of graphitic oxide. *J. Am. Chem. Soc.* **80**, 1339 (1958).
32. Li, D., Müller, M. B., Gilje, S., Kaner, R. B. & Wallace, G. G. Processable aqueous dispersions of graphene nanosheets. *Nature Nanotech.* **3**, 101–105 (2008).
33. Cristina, G.-N. *et al.* Electronic transport properties of individual chemically reduced graphene oxide sheets. *Nano Lett.* **7**, 3499–3503 (2007).
34. Rafiee, J., Rafiee, M. A., Yu, Z.-Z. & Korakar, N. Superhydrophobic to superhydrophilic wetting control in graphene films. *Adv. Mater.* **22**, 2151–2154 (2010).
35. Singh, E. *et al.* Superhydrophobic graphene foams. *Small* **9**, 75–80 (2013).
36. Molla, M. R. & Ghosh, S. Hydrogen-bonding-mediated J-aggregation and white-light emission from a remarkably simple, single-component, naphthalenediimide. *Chem. Eur. J.* **18**, 1290–1294 (2012).
37. Robinsion, J. T. *et al.* Water-scale reduced graphene oxide films for nanomechanical devices. *Nano Lett.* **8**, 3441–3445 (2008).
38. Kenneth, K. S. & Lau, *et al.* Superhydrophobic carbon nanotube forests. *Nano Lett.* **3**, 1701–1705 (2003).
39. Feng, L. *et al.* Super-hydrophobic surfaces: From natural to artificial. *Adv. Mater.* **14**, 1857–1860 (2002).
40. Jang, J.-W. *et al.* Photocatalytic synthesis of pure and water-dispersible graphene monosheets. *Chem. Eur. J.* **18**, 2762–2767 (2012).
41. Wang, X., Zhi, L. & Müllen, K. Transparent, conductive graphene electrodes for dye-sensitized solar cell. *Nano Lett.* **8**, 323–327 (2008).
42. In, K. M., Junghyun, L., Rodney, S. R. & Hyoyoung, L. Reduced graphene oxide by chemical graphitization. *Nature. comm.* **1**, 73–78 (2010).
43. Shen, J. *et al.* Fast and facile preparation of graphene oxide and reduced graphene oxide nanoplatelets. *Chem. Mater.* **21**, 3514–3520 (2009).
44. Youngchao, S. & Edward, T. S. Synthesis of water soluble graphene. *Nano. Lett.* **8**, 1679–1682 (2008).
45. Yu, H., Sheikholeslami, R. & Doherty, W. O. S. Effect of thermohydraulic conditions on fouling of calcium oxalate and silica. *AlchE J.* **51**, 641–648 (2005).
46. Kwark, S. M., Kumar, R., Moreno, G., Yoo, J. & You, S. M. Pooling boiling characteristics of low concentration nanofluids. *Int. J. Heat and Mass Trans.* **53**, 972–981 (2010).
47. Wen, L. & Melendres, C. A. On the mechanism of hematite deposition on a metal surface under nucleate boiling conditions. *Colloids and Surfaces A: Physicochemical and Engineering Aspects* **132**, 315–319 (1998).
48. Ghosh, P. Coalescence of air bubbles at air-water interface. *Chem. Eng. Res. Des.* **82**, 849–8954 (2004).
49. Binks, B. P. *et al.* Particle film growth driven by foam bubble coalescence. *Chem. Comm.* 3531–3533 (2006).
50. Hsu, Y. Y. On the size range of active nucleation cavities on a heating surface. *Trans. ASME J. Heat Transfer* **84**, 207–216 (1962).
51. Lee, Y. & Lo, Y. Highly efficient quantum-dot-sensitized solar cell based on co-sensitization of CdS/CdSe. *Adv. Funct. Mater.* **19**, 604–609 (2009).
52. Jiang, Q. W., Li, G. R. & Gao, X. P. Highly ordered TiN nanotube arrays as counter electrodes for dye-sensitized solar cells. *Chem. Comm.* 6720–6722 (2009).
53. Jo, W. J. *et al.* Phosphate doping into monoclinic BiVO<sub>4</sub> for enhanced photoelectrochemical water oxidation activity. *Angew. Chem. Int. Ed.* **51**, 3147–3151 (2012).
54. Li, G., Wang, F., Gao, X. & Shen, P. Carbon nanotubes with titanium nitride as a low-cost counter-electrode material for dye-sensitized solar cells. *Angew. Chem. Int. Ed.* **49**, 3653–3656 (2010).
55. Seol, M., Kim, H., Kim, W. & Yong, K. Highly efficient photoelectrochemical hydrogen generation using a ZnO nanowire array and a CdSe/CdS co-sensitizer. *Electrochem. Comm.* **12**, 1416–1418 (2010).

## Acknowledgments

This research was supported by the World-Class University (WCU) program (R31-30005) through the National Research Foundation of Korea, funded by the Ministry of Education, Science, and Technology. This work was also funded by the MEST through the National Research Foundation of Korea (No. 2012R1A2A1A01003376, 2012R1A1A2002900 and 2012M1A2A2671779).

## Author contributions

H.S.A. and J.-W.J. designed and performed the experiments and wrote the paper. M.S. measured and interpreted the performance of QDSSCs, and J.M.K. helped fabricate and characterize SFG structures. D.-J.Y. acquired and interpreted XPS and UPS data, and C.P. helped obtain Raman and AFM data. H.K. performed the infrared radiography of nucleate boiling. D.H.Y. and J.Y.K. acquired and interpreted EIS data. G.P., D.I.Y., S.C.P. and J.M.K. helped perform the nucleate boiling experiments, S.E.M. analysis, and contributed to the graphic design of the figures. K.Y. provided comments and assisted in the interpretation of the mechanism. M.H.K. and J.S.L. directed the research project. All authors discussed the results and contributed to the paper.

## Additional information

Supplementary information accompanies this paper at <http://www.nature.com/scientificreports>

**Competing financial interests:** The authors declare no competing financial interests.

**License:** This work is licensed under a Creative Commons Attribution-NonCommercial-NoDerivs 3.0 Unported License. To view a copy of this license, visit <http://creativecommons.org/licenses/by-nc-nd/3.0/>

**How to cite this article:** Ahn, H.S. *et al.* Self-assembled foam-like graphene networks formed through nucleate boiling. *Sci. Rep.* **3**, 1396; DOI:10.1038/srep01396 (2013).